Acta Biomaterialia 8 (2012) 2747–2758

Contents lists available at SciVerse ScienceDirect

Acta Biomaterialia

journal homepage: www.elsevier.com/locate/actabiomat

Variability in the nanoscale deformation of hydroxyapatite during compressive loading in bovine bone

A. Singhal [a,*], J.D. Almer [b], D.C. Dunand [a]

[a] Department of Materials Science and Engineering, Northwestern University, Evanston, IL 60208, USA
[b] Advanced Photon Source, Argonne National Laboratory, Argonne, IL 60439, USA

ARTICLE INFO

Article history:
Received 8 December 2011
Received in revised form 10 March 2012
Accepted 21 March 2012
Available online 28 March 2012

Keywords:
Bone
Synchrotron
Load transfer
X-ray diffraction
Compression

ABSTRACT

High-energy synchrotron X-ray diffraction is used to study in situ elastic strains in hydroxyapatite (HAP) for bovine femur cortical bone subjected to uniaxial compressive loading. Load–unload tests at room temperature (27 °C) and body temperature (37 °C) show that the load transfer to the stiff nanosized HAP platelets from the surrounding compliant protein matrix does not vary significantly ($p < 0.05$) with temperature. This emphasizes that the stiffness of bone is controlled by the stiffness of the HAP phase, which remains unaffected by this change in temperature. Both the extent of hysteresis and the residual value of internal strains developed in HAP during load–unload cycling from 0 to −100 MPa increase significantly ($p < 0.05$) with the number of loading cycles, indicative of strain energy dissipation and accumulation of permanent deformation. Monotonic loading tests, conducted at body temperature to determine the spatial variation of properties within the femur, illustrate that the HAP phase carries lower strain (and thus stresses) at the anterio-medial aspect of the femur than at the anterio-lateral aspect. This is correlated to higher HAP volume fractions in the former location ($p < 0.05$). The Young's modulus of the bone is also found to correlate with the HAP volume fraction and porosity ($p < 0.05$). Finally, samples with a primarily plexiform microstructure are found to be stiffer than those with a primarily Haversian microstructure ($p < 0.05$).

1. Introduction

Bone is composed of an organic phase (mainly type-I collagen), a mineral phase (calcium hydroxyapatite, $Ca_6(PO_4)_3(OH)_2$ or HAP) and water. These basic components are organized and assembled to form the different hierarchal levels of bone [1]. The HAP phase in bone is usually non-stoichiometric with 4–6% (by weight) carbonate ions substituting for phosphate ions [2,3]. At the macroscopic level, bone is of two types: cortical bone (examined in the present study), which is the dense outer layer of whole bone, and trabecular bone, which is the inner porous region of whole bone. At the microscopic level, cortical bone made up of a number of cylindrical motifs called osteons, each of which contains a central Haversian canal running through its entire length, and aligned with the longitudinal direction of bone. The osteons are made up of concentric sheets of lamellae, which are made up of collagen fibril bundles arranged in various configurations, depending on the structural and functional requirements of the species [1,4]. Water is located at multiple hierarchical levels—in the triple helical collagen molecules, in the collagen fibril and in fibril gaps—mediating mineral–organic interactions [1,5–7]. At the nanoscopic level, bone is modeled as a composite, with HAP, collagen and water as the main constituent phases. HAP is observed as platelets with approximate size $50 \times 25 \times 4$ nm, as determined by X-ray diffraction (XRD) [8,9]. A number of composite models have been proposed to describe the interaction of these two phases and to study their contribution to the bulk behavior of bone. One widely accepted model, which is also used in the present work, suggests that HAP platelets are present as nanoreinforcements distributed throughout a matrix of collagen and water [10–13]. Another model reported recently suggests that HAP and collagen are present as continuous phases and form an interpenetrating composite [3,14,15]. This structure, if confirmed, would necessitate a different model, which is beyond the scope of the paper.

Most mechanical tests conducted so far on bone have focused on the macroscopic-level properties [16–20]. To shed light on the role of the individual phases in the deformation of bones, stresses in the HAP and collagen phases at the lowest level of the structural hierarchy of bone must be measured. Scattering using high-energy, high-intensity X-rays from synchrotron sources provides elastic strain information from phases with sizes as small as few nanometers, averaged over volumes as large as a few cubic millimeters (using a large, unfocused X-ray beam) or as small as a few cubic micrometers (using a focused beam) [21]. This method has been used extensively to study load transfer between matrix and

* Corresponding author. Tel.: +1 847 467 5416; fax: +1 847 491 7820.
E-mail address: AnjaliSinghal2007@u.northwestern.edu (A. Singhal).

1742-7061/$ - see front matter © 2012 Acta Materialia Inc Published by Elsevier Ltd. All rights reserved.
http://dx.doi.org/10.1016/j.actbio.2012.03.036

reinforcement in synthetic composites (e.g., Refs. [21–24]). The in situ diffraction-based measurement of elastic strains in the phases of a composite allows a description of load partitioning between the phases as a function of the applied stress, strain and/or time for various environments (temperature, irradiation).

Synchrotron XRD has been widely used in the past to study strains in natural, non-mineralized tissues such as tendon [25–31], and has been applied only recently to mineralized biological composites such as bones [8,13,32–43], teeth [44–47] and antler [41,34]. In situ compression testing has been used in combination with high-energy synchrotron X-ray scattering in bone in a number of recent studies [8,32,39,40,42,48]. The internal strains are quantified at the atomic level (through changes in lattice constants) in the HAP phase by wide-angle X-ray scattering (WAXS) and at the fibrillar level (through changes in the periodic spacing of the HAP crystals within the collagen fibrils) by small-angle X-ray scattering (SAXS). The elastic load partitioning in the HAP phase and the elasto-plastic strain in collagen fibrils were studied during monotonic loading of a canine fibula in Refs. [8,32]. Diffraction measurements have been performed on bovine plexiform bones to study the load transfer between the woven and the lamellar components of the bone [48]. This technique has also been used to study the deformation evolution in deer antler trabecular bones, which revealed the change in the strain distribution with the trabeculae orientation and applied stress [34]. A combination of WAXS, SAXS and macroscopic strains has been used to study the post-yield mechanics of human cortical bones in compression [42]. In another recent study, the effect of irradiation dose on the load-induced strains in HAP and fibrils in bovine bone was determined, and it was shown that the residual strains in the HAP phase after unloading decreased with dose as a result of damage at the HAP–collagen interface [39]. During tensile testing of bone [35–37], in situ synchrotron XRD showed that the tissue, fibril and HAP take up successively lower levels of strains at a given stress, suggesting a gradation of properties at the different hierarchical levels, where the stiff reinforcement HAP phase at smaller length scales is embedded in a softer protein matrix phase. Beyond the yield point of the tissue, the fibrils remain under constant stress as a result of load transfer by shear from the frictional sliding of the fibrils and the inter-fibrillar matrix. Finally, in a study on bovine dentin, which is also made up of mineralized collagen fibrils, the variability of HAP apparent modulus (ratio of applied stress and HAP elastic strain) was characterized across different locations in the root dentin [47]. Freeze–thaw cycles were shown to have a negligible effect on the apparent HAP modulus of bovine dentin [44].

The apparent modulus is the ratio of the applied stress and phase strain, and provides a description of the load partitioning between the component phases of a composite. The Young's modulus of HAP is 114 GPa [49,50], whereas that of collagen is 1 GPa [51]. During elastic loading of bone, stresses are expected to be transferred from the less stiff matrix to the stiffer HAP reinforcement, resulting in an increase in HAP strains and a concomitant decrease in the collagen strains compared with the strains developed upon loading these phases individually. The higher HAP strains result in an apparent modulus lower than the Young's modulus, measured by synchrotron XRD as 38 ± 0.5 GPa for canine bone [52], 27.3 ± 2.0 GPa for bovine bone [39] and 26.5 ± 7.2 GPa for bovine dentin [47]. A lower bound estimate of the HAP apparent modulus can be obtained from the upper bound for strain using a Voigt model for a HAP–collagen composite. This value is found to be 47 GPa, using volume fractions determined by thermo-gravimetric analysis and the Young's moduli of HAP and collagen [39]. This lower bound is significantly higher than the experimental values determined above; this discrepancy points to the fact that biologically derived HAP has a significantly lower Young's modulus compared with inorganic HAP and, as shown in Ref. [45], a value <65 GPa has to be invoked for the Young's modulus of biologically derived HAP in order to justify the low experimental values of the apparent modulus. This low Young's modulus can be justified by changes in the HAP platelet composition as a result of carbonate substitution, a nanocrystallite size and surface adsorption, as discussed in detail in Ref. [45].

An added complexity in the study of biological materials is the variability of samples from one location to another. These variations are introduced during the growth and development of the bone and may be affected, among other things, by the local in vivo loads experienced at its location. The variations can be at the constituent phase level (e.g., different volume fractions) [53,54], or at a higher level (e.g., porosity, microstructure and orientation) [55–58]. Thus, testing samples from different locations within bone can lead to high property variability, so that a large number of samples must be tested to get statistically repeatable properties. Many researchers have shown that the macroscopic properties of bone vary along the length as well as across different quadrants within the human, bovine and mouse femurs [59–65]. There is general agreement that the medial and lateral quadrants are stiffer than the anterior and posterior quadrants, and that the mid-diaphyseal region is stiffer than the epiphyses. Also, the porosity of bone is found to increase from the periosteum to the endosteum and at varying gradients in bones from different mammalian species [53,55,64]. Additionally, studies have shown that the posterior quadrant of the human femur has a higher porosity compared with other quadrants [53,61,64,66]. The mechanical properties of bone also depend on the environment in which testing is conducted. It has been found that bone has lower fracture toughness at higher temperatures [67], and it is stiffer when tested in dry conditions [7]. It is thus important to characterize its properties under correct external conditions: hydrated and at body temperature.

Here, a quasi-static load/unload scheme (similar to that used in Refs. [19,68]) is applied to bone samples to investigate the energy dissipated during hysteresis as a result of permanent deformation during loading–unloading cycles at room and body temperatures. The in situ phase strains measured by synchrotron X-ray scattering during these loading schemes is used in conjunction with information obtained from thermogravimetry, ultrasonic speed measurements and microscopy, to characterize and understand both inter- and intra-sample variability for the first time, between samples collected from various regions in a bovine cortical bone.

2. Materials and methods

2.1. Materials

Fresh bovine femurs of 18-month-old Black Angus cows, obtained from the Aurora Packing Company (Aurora, IL) ~5 h after death, were cleaned of their blood, ligament tissues and bone marrow. At all times, the bone was maintained in a hydrated condition to minimize property changes as a result of dehydration [7]. Samples ~5 mm high (oriented within 0–10° of the long direction of the bone axis) and ~4 × 3 mm^2 cross sections were cut with a diamond wafering blade under constant irrigation with water. All the samples were taken from the mid-diaphyseal region of the hind leg right femur of a single animal. The dimensions of the cut samples were measured with a point micrometer, and their weights were determined in air using a micro-balance, after blotting out the surface water. The ratio of the weight and volume of the samples is taken to determine the apparent density of all the samples. The samples were then stored in phosphate-buffered saline (PBS) and frozen at −20 °C until the time of the diffraction experiment. This

freeze–thaw treatment has been shown to have no effect on the measured properties in bovine dentin [44], which is also made up of collagen fibrils similar to bone.

2.2. X-ray scattering measurements

As reported in previous studies [39,40,44,45,47], uniaxial compression tests were performed on a hydraulic load frame at beamline 1-ID of the Advanced Photon Source (Argonne National Laboratory, Argonne, IL). A schematic of the experimental setup is shown in Fig. 1. Load was applied parallel to the height of the sample (and thus along the long axis of the femur, which also coincides with the longitudinal orientation of osteons, as shown in the inset in Fig. 1), corresponding to the *y*-axis in the laboratory frame of reference. A hydration system consisting of vinyl tubing was filled with PBS, to keep the sample hydrated throughout the experiment. The PBS was circulated through an external temperature bath with a peristaltic pump, which maintained the sample bath at room temperature (27 °C, RT) or body temperature (37 °C, BT) for the experiments, as monitored with a thermocouple. The samples spent at least 5 min (and often 10 min) between the time they were immersed in the heated PBS and the time the first XRD data were collected. A control experiment where temperature was measured by a thermocouple embedded in the center of a bone sample (originally at room temperature) immersed in 37 °C PBS indicated that ~2 min are sufficient to reach thermal equilibrium in the sample within 1 °C.

As in previous studies [39,40,44,45,47], a parallel beam of monochromatic X-rays (70 keV energy corresponding to a 0.178 Å wavelength) with a $50 \times 50\ \mu m^2$ cross section was transmitted through the sample perpendicular to the direction of applied load (i.e., parallel to the *z* direction, sampling a volume of $0.0075\ mm^3$ per measurement), as shown in Fig. 1. Only WAXS measurements were taken in this study, since the low exposure times essential to minimize the irradiation dose on the samples resulted in poor SAXS signal from the scattering of the regular spacing between the HAP crystals [39]. The WAXS patterns were recorded with a GE 41-RT flat panel detector (2048×2048 pixels, $200\ \mu m^2\ pixel^{-1}$) placed at a distance of 1490 mm from the specimen. Each sample was first centered using absorption measurements to find the vertical and horizontal centers of the sample. Measurements were made in two rows of five locations each. The measurements in the *x* direction were separated by a distance of 0.5 mm; two locations each were measured to the left and right of the locations measured at the horizontal center. In the *y* direction, the rows were 0.5 mm above and below the vertical center of the sample. All ten locations were measured at each load increment. The samples were exposed to X-rays for 1 s to collect diffraction data, resulting in an average radiation dose of ~0.3 kGy for each strain measurement. Such relatively low doses do not affect the strain measurements, as previously reported [39]. Ceria (CeO_2, NIST Standard Reference Material SRM 674-a) was used as a reference material to calibrate the WAXS parameters (specimen–detector distance, beam center, detector tilts).

Two series of uniaxial compression experiments were performed under load control. The loads were applied within a period of 1 s and held constant during data acquisition and sample translation, resulting in a total of 1.5 min at each load. In the first series, eight samples (four each at 27 and 37 °C, labeled R1–4 and B1–4 respectively) were repeatedly loaded and unloaded with −5 MPa steps between a minimum stress of 0 MPa and a maximum stress σ_{max}, which was increasing from −30 to −100 MPa in −20 MPa increments over five consecutive load–unload loops. A total of ten WAXS patterns were collected at each loading and unloading level, one for each of the ten locations. The second series of experiments were done at 37 °C, and involved a single load–unload loop on 19 different samples, taken from different quadrants on a femur cross section. These samples were loaded in eight steps of −7 MPa up to a maximum of −60 MPa with WAXS measurements at each load level over each of the ten locations.

2.3. X-ray scattering data analysis

Longitudinal strains in the mineral HAP phase were determined from WAXS patterns, as previously described in detail [8,39,40,44,45,47]. Each WAXS diffraction pattern was converted from Cartesian to polar coordinates, over the entire 360° detector azimuth (η) with an azimuthal bin $\Delta\eta = 10°$, and the diffraction peak of interest (hydroxyapatite (00.2) in the present study) was fit to a pseudo-Voigt function. The resulting peak centers r_{hkl} were plotted vs η for different applied stress levels and found to intersect at a single point, corresponding to the invariant radius (r^*) [32]. The measured radii r_η were then referenced to this invariant radius value to give the elastic strain ε_η as a function of orientation as

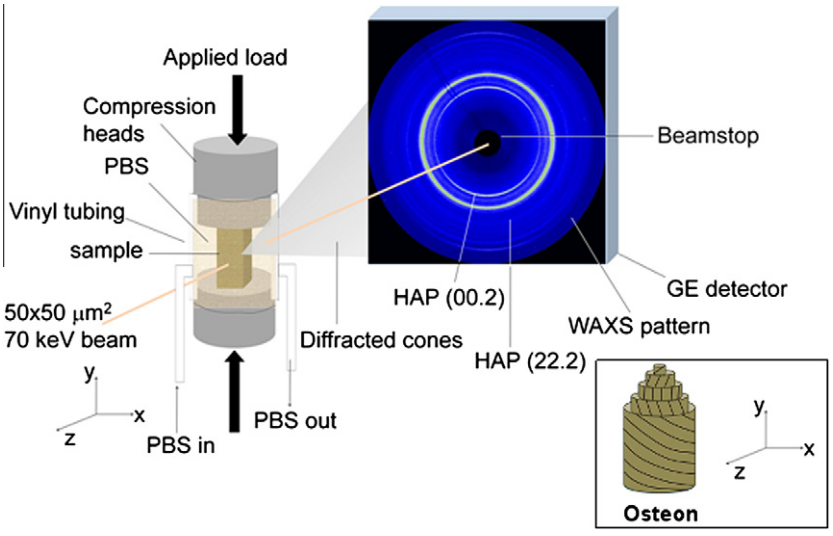

Fig. 1. Schematic of the setup used to collect synchrotron XRD data on uniaxially loaded bone samples under hydration and temperature control. The inset shows the orientation of osteons with respect to the loading direction in the sample.

$$\varepsilon_\eta = (r^* - r_\eta)/r_\eta \quad (1)$$

The strain profile was fit to a biaxial strain model and used to derive the strain components along the longitudinal orientation (ε_{yy}, $\eta = 90/270°$) [69]. Other strains, in particular the strain in the transverse orientation as a result of the Poisson's effect (ε_{xx}, $\eta = 0, 180°$) can also be determined, but are not reported here. Using this analysis, the longitudinal strain in the HAP at zero stress ($\varepsilon_{yy,0}$) is obtained, both before and after deformation. The ratio of the applied, uniaxial stress σ_{app} to the longitudinal lattice strain ε_{yy} (in the following, the short-hand notation ε is used) gives the apparent modulus ($E_{app} = \sigma_{applied}/\varepsilon$). This is calculated by taking a linear best fit of the loading part of the stress–strain (σ_{app} vs ε) curve. Not used for this best-fit slope determination were data points either at the highest or lowest stresses (one to three such points), such that at least five data points were used for slope determination, and the fits produced a maximum value of r^2.

The mean HAP (00.2) peak intensity was used to obtain a measure of mineralization within the diffracting volume. For this purpose, the HAP (00.2) mean peak intensity (integrated over the full diffraction ring) was normalized with the transmitted intensity, which takes into account both the diffracted and absorbed intensity, and the sample thickness [70]. This intensity ratio, referred to as the HAP index, was calculated as an average of the ten locations measured.

2.4. Ultrasonic stiffness measurements

Ultrasonic sound velocity measurements were performed to determine the Young's modulus of the samples, as discussed previously in Refs. [39,71,72]. The velocity of the ultrasonic pulse was calculated by determining its time of flight (TOF) through a known thickness of the sample, which is the entire height of the sample in this case. This is done with the simplified assumption that the entire sample height consists of the same microstructure or the same distribution of microstructures. The samples were mechanically coupled to two 5 MHz transducers with molasses. Pulses were generated in the longitudinal and shear modes, and directed along the longitudinal direction of the samples, which corresponds to the long axis of the femur. The output from the second transducer was recorded by the Matec software (MUIS-32), and the TOF was calculated. Three repeat measurements were made in each of the longitudinal and shear modes to calculate the longitudinal (V_l) and shear (V_s) velocities, respectively. These were then used along with the density ρ (calculated as the ratio of the mass and volume of the sample, measured as described in Section 2.1) to calculate the Young's modulus E and Poisson's ratio ν, according to

$$V_l = \sqrt{E(1-\nu)/\rho(1+\nu)(1-2\nu)} \quad (2a)$$

$$V_s = \sqrt{E/2\rho(1+\nu)} \quad (2b)$$

The above formulae are for calculating the Young's modulus of an isotropic material, whereas bone is an anisotropic material. However, for this measurement, bone is assumed to be isotropic as a simplification. This is justified to some extent because the values of the longitudinal Young's modulus determined above are within 7% of the values obtained with an orthotropic assumption [73].

2.5. Thermogravimetric analysis

Thermogravimetric analysis (TGA) was performed to determine the volume fractions of the three main phases (HAP, collagen and water), using a Mettler Toledo instrument calibrated with pure In and Al. The TGA samples (3–10 mg) were cut from the samples after the X-ray experiments, approximately from the region sampled by the X-ray beam. They were heated from 25 to 680 °C at a rate of 10 °C min^{-1} in air, in accordance with an earlier study [74]. The TGA curves, showing the sample mass as a function of temperature, exhibit three distinct regions. The first is a gradual slope, corresponding to water loss, up to ~205 °C and ending in a plateau. The plateau then slopes down during the collagen loss and ends in another plateau at ~545 °C. Heating beyond that temperature results in a further mass loss, owing to decomposition of the carbonate from the mineral phase. The first derivative of the mass loss was plotted as a function of temperature to get the start and end of the phase decompositions. Calculating the difference in the mass of the sample between two transition temperatures (25, 205 and 545 °C) gives the weight fractions of water, collagen and HAP. The weight fractions were then converted to volume fractions using densities of 1 g cm^{-3} for water, 1.1 g cm^{-3} for collagen and 3.2 g cm^{-3} for HAP [75].

2.6. Microstructure determination

Cross sections perpendicular to the longitudinal direction of the sample (in the x–z plane) were prepared from the mechanical test samples. They were polished using diamond lapping films with grit sizes 3, 1 and 0.5 μm in decreasing order, and imaged using an optical microscope with a 60× magnification. Representative micrographs are shown in Fig. 2. The samples structures span purely Haversian and purely plexiform structure. They were assigned a zero value for a completely plexiform structure and a unity value for completely Haversian structure. An intermediate number between zero and unity was assigned for a mixture of the two structure types, based on visual estimations. The osteons in the Haversian structure and lamellae in the plexiform structure are oriented parallel to the y-axis direction (longitudinal direction of sample) in Fig. 1.

2.7. Statistical analysis

One-way analysis of variance (ANOVA) was performed using Origin software (OriginLab, Northampton, MA) to test for the significance of variations in (i) the apparent HAP modulus and the hysteresis as a function of the loading cycles and temperature in the cyclic loading experiments, and (ii) the apparent HAP modulus as a function of the anatomical location of samples in the repeatability analysis.

3. Results

3.1. Cyclic loading tests

Fig. 3a shows a plot of the applied stress vs HAP lattice strain for one location of sample R3 (representative of the nine other locations measured) for the five load–unload cycles. Similar curves were obtained for R1, R2, R4 and B1–4. The HAP strain magnitudes increase near linearly with stress, indicating elastic behavior, but they are greater during unloading than during loading, for a given applied stress, at all loading cycles for 75% of all the locations measured in the samples (80 locations measured in all). The only exceptions to this hysteretic behavior are the fourth and fifth load–unload cycles for which, for a given stress, the strain magnitude during unload is less than that during load for almost half the locations (40% and 60% for the fourth and fifth cycle, respectively) and greater than that during load for the other half, in no systematic order. The loading curve of the fourth cycle shows a significant deviation from linearity towards more compressive strains at −70 MPa. The loading curve of the fifth cycle shows a steep increase

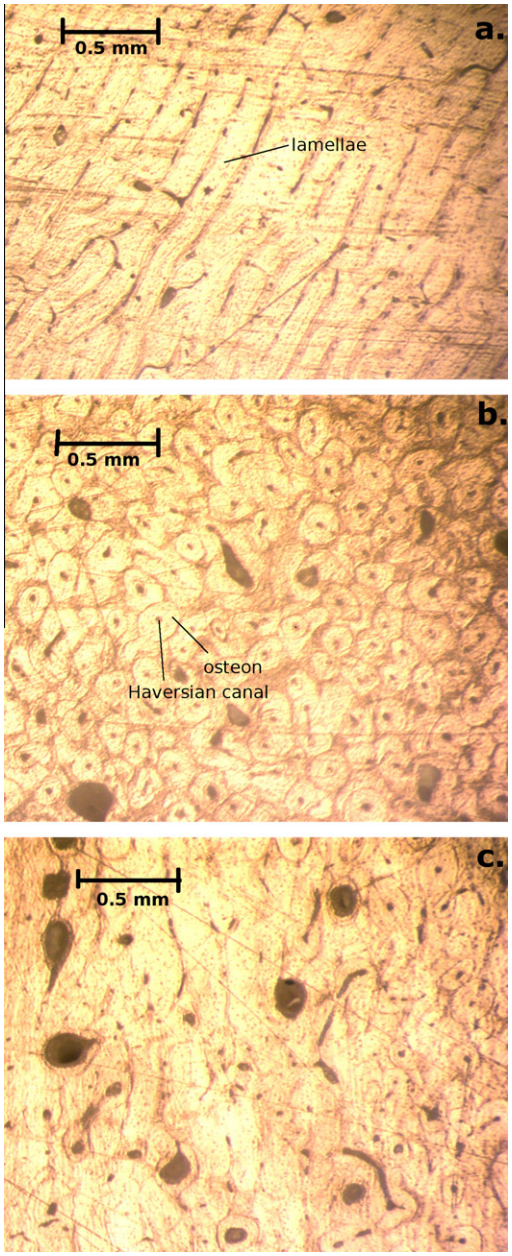

Fig. 2. Optical micrographs of cross section of bovine bone showing (a) plexiform microstructure with a lamellar unit indicated (microstructure index 0), (b) Haversian microstructure with a Haversian canal and osteon indicated (microstructure index 1) and (c) mixed type microstructures (microstructure index 0.5).

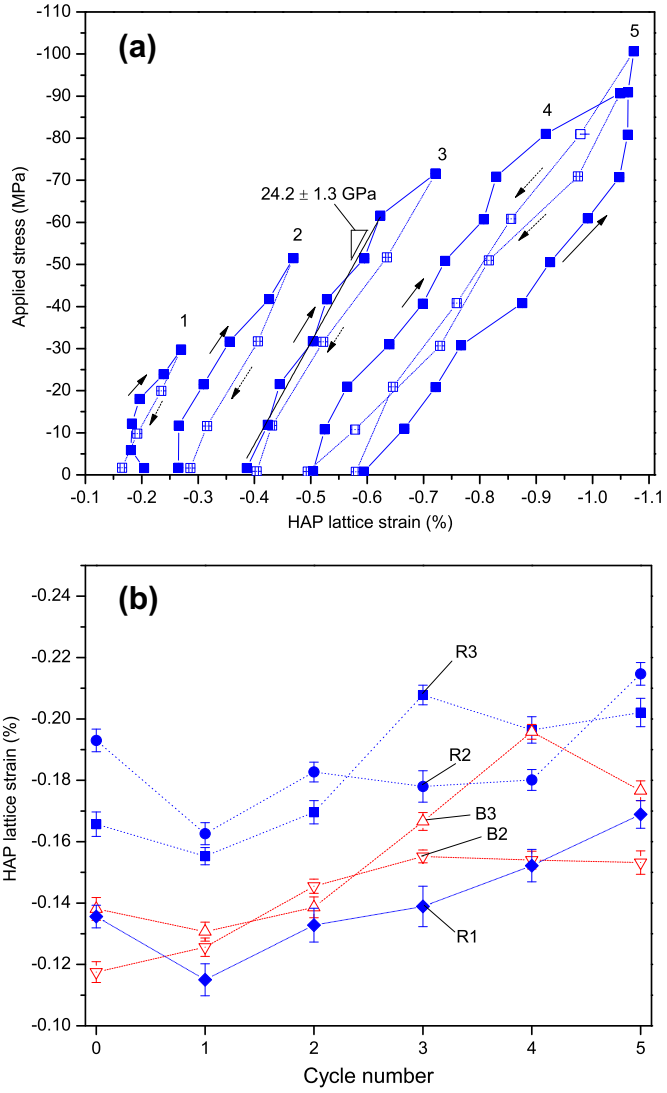

Fig. 3. (a) Plot of applied stress vs HAP lattice strain at room temperature (sample R3) showing five load–unload loops (filled and hollow symbols, respectively), showing hysteresis. Loops 2–5 are each offset along the *x* axis by 0.1% for clarity. A best-fit line on the loading segment of the third loop shows the apparent modulus determination. (b) Plot of the HAP residual strains as a function of loading cycles for five different samples (filled and hollow symbols are, respectively, for room and body temperature).

in strains with stress at −70 MPa. The area within each hysteretic loop (referred to in the following as the hysteresis) was calculated for individual locations in all the samples. ANOVA showed that there is no significant difference between the hysteresis of the RT and BT samples, for a given maximum stress, at $p < 0.05$. Combining samples from both temperatures and comparing the hysteresis between the individual cycles, it was found that the hysteresis increases with increase in cycles, as expected from the increase in maximum stress, at $p < 0.05$, the only exception being the hysteresis of the fourth cycle, which is not significantly different from the fifth cycle. The average variation in the total hysteresis (sum of all the loops) of the ten locations within any single sample is 36%.

The HAP residual strains were found to increase in magnitude with increase in loading cycles, as reported in Fig. 3b, where representative residual strain vs cycle plots are shown for five different samples. The increase in residual strains is not found to be completely systematic for all samples, as in samples R1 and R2, where the strains decrease after the first cycle and increase after subsequent cycles. Three samples (R1 and B1 and B4) were fractured early during the experiment, resulting in their having only three complete load–unload loops. These samples were eliminated from the group of samples which had five full load–unload loops, and compared separately. Neither group showed statistically significant difference in the change in residual strain, from the beginning of the experiment to the end, between the RT and BT samples. The change in the residual strain varies greatly within a single sample among the ten locations measured, as well as between samples. The average increase in the magnitude of the residual strains is ~19% over all the locations for the samples which accumulated five full load–unload loops.

The HAP apparent modulus was calculated by taking a best-fit line on the loading segment of the stress–strain curves. Since the WAXS data were acquired at an exposure of 1 s to minimize the irradiation dose, the intensity count statistics were poor compared

with most previous studies, and the peak fits (and thus strains) had large errors in many cases. In calculating the apparent moduli, thus only those plots were taken for which the best-fit procedure provided a linear regression coefficient value $r^2 > 0.95$; this corresponded to 245 apparent moduli out of 370 stress–strain curves. A histogram of these 245 apparent moduli showed that the lowest value was a clear outlier, which was thus eliminated. The remaining 244 apparent moduli, with an average value of 24.7 ± 10.9 GPa, were then split into two groups according to the test temperature. ANOVA showed that no significant difference existed between the two groups, at a 95% confidence level. The moduli were then compared, based on their cycle numbers. No significant difference ($p < 0.05$) was found for any pair of subsequent cycles.

3.2. Repeatability study

3.2.1. Spatial variations

Samples obtained from various quadrants of the femur were monotonically loaded up to −60 MPa, to determine the variability in the HAP apparent moduli. They are named according to their location—anterio-medial (AM), anterio-lateral (AL) or posterior-lateral (PL)—and a number corresponding to the order in which they were extracted. The E^{app}_{HAP} of the samples in the cyclic loading study in Section 3.1 (samples R1–R4 and B1–B4) are also included in this repeatability analysis and renamed according to the aforementioned naming convention. Additionally, seven samples from a previous study [39] are included here; they were subjected to 3–3800 kGy of irradiation, but can be combined with the present data, because these levels of irradiation were found to have no effect on E^{app}_{HAP} [39]. For those samples with ten measurement locations (AM1–4, AM7–12, AL1–6, PL1–4 and PL7–9), the measurements along a single column were averaged to get five apparent moduli per sample. The results of statistical analysis using ANOVA are shown in Table 1. The samples were first grouped according to their anterior or posterior location. There was no significant difference between the anterior and posterior E^{app}_{HAP} values at $p < 0.05$ level. The same samples were then grouped according to their location on the medial or lateral side of the femur. ANOVA showed that the E^{app}_{HAP} values at the medial side were significantly greater than those at the lateral side at $p < 0.05$. The E^{app}_{HAP} values were further subdivided into the quadrants AM, AL or PL from which they were obtained. Pairwise ANOVA of these groups showed that the moduli in AM were significantly greater than those in AL. According to the microscopy analysis, the samples obtained from the AM and AL quadrants of the femur had a mixture of Haversian and plexiform microstructures, whereas the samples taken from the PL quadrant had primarily plexiform structure.

Table 1
Groups of apparent HAP moduli listed with their mean and standard deviations; p-values of the statistical comparison using ANOVA between groups are also listed.

Group	Mean ± std dev. (GPa)
Anterior (Ant)	28.2 ± 7.7
Posterior (Post)	29.0 ± 4.1
Medial (Med)	29.0 ± 7.4
Lateral (Lat)	26.3 ± 5.6
Anterio-medial (AM)	29.0 ± 7.4
Anterio-lateral (AL)	25.4 ± 6.8
Posterio-lateral (PL)	27.0 ± 4.5
Comparisons	p-Value
Ant vs post	Ant ≈ Post ($p = 0.55$)
Med vs lat	Med > Lat ($p = 0.02$)
AM vs AL	AM > AL ($p = 0.03$)
AM vs PL	AM ≈ PL ($p = 0.14$)
AL vs PL	AL ≈ PL ($p = 0.26$)

Depending on the orientation of the sample in the femur cross section, the X-rays traversed the samples across the thickness of the femur radially or circumferentially. Since multiple locations were measured on all the samples, those samples were separated from the pool, which contained locations measured from the periosteum to the endosteum, to determine the variation in properties across the femur thickness or radial variation. The E^{app}_{HAP} values were plotted in order of measurement from the periosteum to endosteum, separately for samples obtained from different quadrants. No systematic and statistically significant trends were found from the periosteum to the endosteum at $p < 0.05$ in any of the quadrants measured.

Finally, E^{app}_{HAP} values were arranged according to the location from which they were obtained in the femur cross section and plotted as a function of angle, with the reference angle being 0° at the anterior side of the femur and increasing angles in the clockwise direction, as shown in the inset in Fig. 4. Young's modulus E obtained through ultrasonic measurements is also plotted as a function of the angle in this figure. Young's modulus could not be obtained for the four samples which had been crushed during mechanical testing (AM1, AL4, AL6 and PL2). Fig. 4 shows that E^{app}_{HAP} remains constant, within error, between 0° and 30°, 120° and 180° and 270° and 360°, but is lower between 40° and 90°. There is no information about the posterior-medial region (180–270°) in this study (indicated by the break in the x-axis in the figure). The average E^{app}_{HAP} is 27.4 ± 4.8 GPa, using all samples studied here. The average variability between the E^{app}_{HAP} values at the different measurement locations in a single sample is ∼15%. Young's moduli E values show a similar trend of lower values in the anterio-lateral region (the two data points between 30° and 120°). The average E value is 20.5 ± 1.5 GPa, using all the samples studied here.

3.2.2. Correlations

Fig. 5a shows the samples plotted with their E^{app}_{HAP} in order of increasing magnitudes, with the corresponding E values; the corresponding HAP volume fractions and the sample apparent densities are plotted in Fig. 5b. The uncertainties in the volume fractions were determined by performing repeat TGA measurements on samples taken from adjacent locations on three mechanical test samples, and are only indicative, given the sample-to-sample variation. The average volume fractions are 39.8 ± 2.8%, 37.5 ± 1.3% and 22.8 ± 2.6% for HAP, collagen and water, respectively, evaluated over all the bone samples in this study. A comparison of the volume fraction of HAP (V_{HAP}) between the AM, AL and PL quadrants shows that the AM quadrant has a higher V_{HAP} than AL at $p < 0.05$. No statistically significant differences exist between V_{HAP} for other quadrants. Fig. 5c shows E^{app}_{HAP} and E values plotted with their corresponding microstructure indices; the modulus decreases with increase in the volume fraction of the osteonal content in the microstructure.

Table 2 lists the correlation coefficients of pairs of variables along with the type-I error probabilities, resulting in the observed variability between the samples. Type-I error indicates the probability (p-value) of getting the correlation coefficients by chance. The variables studied here are the volume fraction of HAP (V_{HAP}), the volume fraction of collagen (V_{coll}), the density of the sample, their Young's modulus E, the intensity index of HAP and the sample microstructure, as defined by a zero value for a completely plexiform structure and a value of unity for a completely Haversian structure. At $p < 0.05$ confidence level, the E^{app}_{HAP} exhibits strong positive correlation with the HAP volume fraction ($R = 0.42$) and the HAP intensity index ($R = 0.47$), weak positive correlation with Young's modulus ($R = 0.1$) and the density of the sample ($R = 0.33$), almost no correlation with the collagen volume fraction ($R = -0.07$), and weak negative correlation with the sample

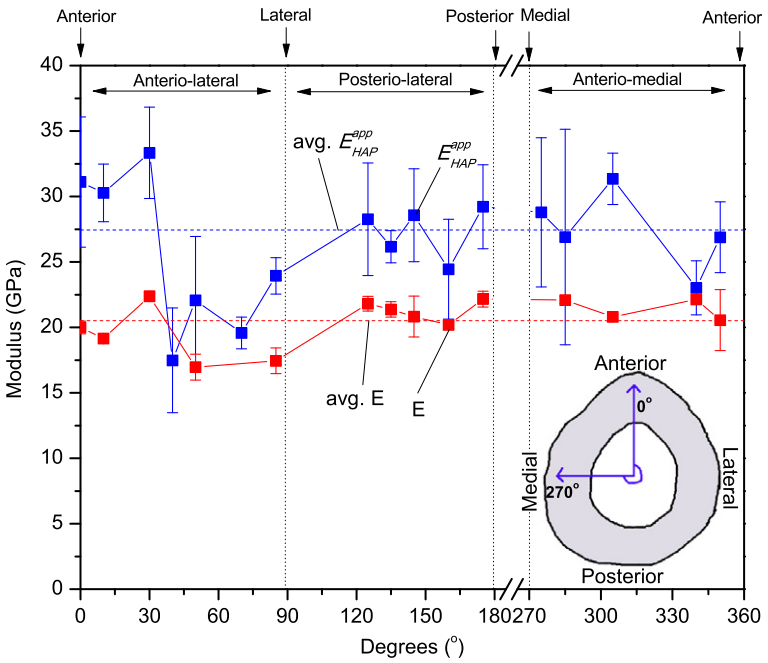

Fig. 4. Plot of the HAP apparent modulus and bone Young's modulus as a function of the sample orientation with respect to the anterior direction. The error bars on HAP apparent modulus represent standard deviation between the moduli measured at different locations on the sample (n = 3 or 10). The error bars on Young's modulus represent the standard deviations propagated from three repeat measurements of the time of flight of the ultrasonic pulse. The data points at 40°, 85°, 175°, 275° and 305° are average of data from two samples and that at 70° is an average of six samples. These samples were radially located with respect to each other on the femur cross section and are averaged to represent a single point. The inset shows a femur cross section with the angles indicated.

microstructure (R = −0.33). Young's modulus, in contrast, is well correlated with the mineral volume fraction (R = 0.83) and apparent density (R = 0.86) and negatively with the collagen volume fraction (R = −0.83) and the sample microstructure (R = −0.73) at p < 0.05 confidence. The microstructure of the samples is negatively correlated with the apparent density (R = −0.64) at p < 0.05. An increase in the HAP volume fraction results in an increase in the sample apparent density (R = 0.96) and a decrease in the collagen volume fraction (R = −0.47) at p < 0.05 confidence. The HAP volume fraction also exhibits weak correlation with the HAP intensity index (R = 0.11).

4. Discussion

4.1. Cyclic loading experiments

4.1.1. Hysteresis and apparent modulus

The load–unload curves (Fig. 3a) show that the magnitude of elastic strain (and thus stress) carried by the HAP phase increases mostly linearly with the applied stress, as expected for a composite showing load transfer between elastic phases. The greater HAP strain magnitude measured during unload suggests that permanent deformation takes place in the matrix collagen phase during the loading period which is not recovered during unloading. In other words, all the elastic energy stored in the HAP phase during the loading cycle is not recovered during the unloading cycle, resulting in deformation hysteresis. This residual elastic strain indicates that the collagen deforms during the load–unload cycle, plastically (and thus permanently), and/or viscoelastically [76,77] with the possibility of recovery with time [78]. In a recent finding by Gupta et al. [79], it was shown that the calcium mediated charged interactions within the extra-fibrillar matrix is the rate-limiting step for plastic deformation in bone. These interactions form a plastic "glue" between the fibrils and are sacrificial in nature [80,81]. Charged interactions are present at the extra-fibrillar level as well as the intra-fibrillar level, between HAP and non-collagenous proteins and HAP–collagen, respectively [82]. A systematic increase in apparent modulus of HAP with cycle number would be expected if there were any loss in these charged interactions at the intra-fibrillar level (e.g., delamination at the HAP–collagen interface), because collagen would transfer less strain to the HAP platelets for a given applied stress. Such damage is found to occur during irradiation with high-energy X-rays, and is suggested to take place as a result of breakage of ion-mediated bonds between HAP and collagen [39,83]. However, unchanged moduli with cycle numbers suggest that the damage at the HAP–collagen interface does not occur or recovers upon unloading. Fibrillar level yielding has been shown to occur at stresses between 60 and 80 MPa, and is hypothesized to occur as a result of the formation of diffuse microcracks axially along the fibrils [35]. The deformation and yielding of collagen molecules occurs by stretching of triple helices, followed by an increase in the gap region and, ultimately, sliding of neighboring triple helices with respect to each other [29]. The collagen matrix thus undergoes viscoelastic or permanent deformation without interfacial delamination, and results in the HAP unload curve having a greater strain magnitude than the loading curve, as illustrated for the first four cycles in Fig. 3a.

Hysteresis has been observed to different extents in the eight samples studied here, with an average variation of 36% between the ten locations in any single sample. Variations can arise within a sample for various reasons, e.g., different degrees of mineralization, HAP crystal orientation and porosity. Collagen will undergo yielding or permanent deformation, depending on the local stiffness of the region being probed. The fourth and fifth loading cycles show the maximum variability in the position of their unload cycles with respect to the loading cycle, i.e., whether the magnitude of the strains during unloading are greater or less than that during loading. This suggests that, during this load cycle where the

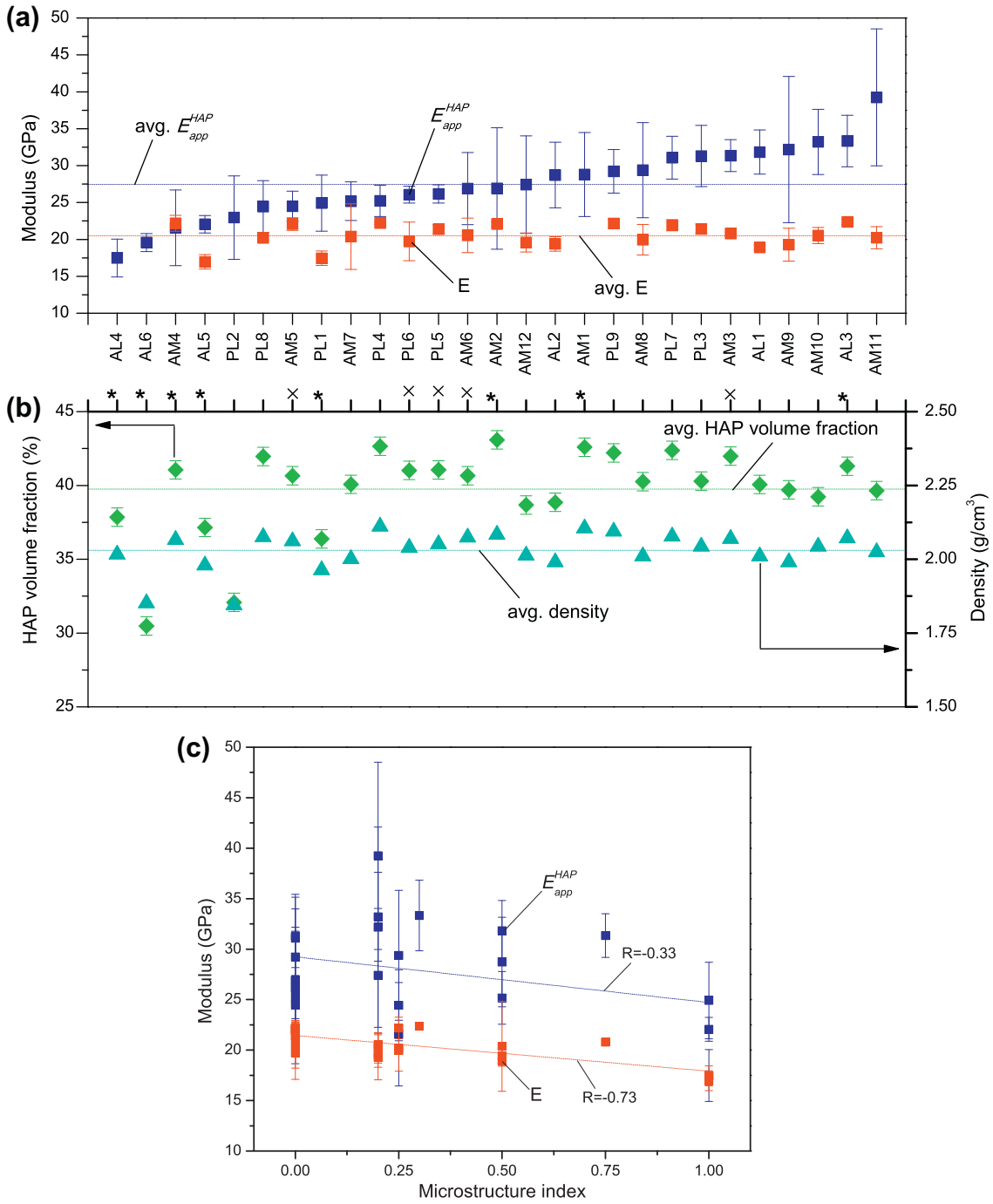

Fig. 5. (a) Plot of the apparent HAP moduli arranged in order of increasing magnitude, along with the associated Young's modulus. Each data point is obtained from a single sample. The error bars on HAP apparent modulus represent standard deviation between the moduli measured at different locations on the sample (n = 3 or 10). The error bars on Young's modulus represent the standard deviations propagated from three repeat measurements of the time of flight of the ultrasonic pulse. AM, AL and PL indicate samples obtained from the anterio-medial, anterio-lateral and posterior-lateral locations respectively. (b) Corresponding plot of sample density and HAP volume fractions. The samples from the load–unload experiments (R1–4 and B1–4) are indicated with stars next to their labels, and the samples from previously published experiments [39] are indicated with a cross. (c) Plot of apparent HAP and Young's modulus vs the microstructure index. The dotted lines indicate the correlation between the modulus and microstructure.

maximum load reaches −90 MPa, the matrix has a greater tendency to yield, and interfacial delamination between HAP and collagen can occur in some cases. Delamination at the HAP–collagen interface may occur during loading up to stresses as high as −100 MPa when the interfacial bonds (electrostatic, hydrogen or Van der Waals type) are broken owing to the shear stresses generated during load transfer. This would then allow the collagen molecules to slide at the HAP–collagen interface [27–29,84] and result in a reduction in stress and strains transferred from the collagen matrix to the HAP platelets. This is seen when the HAP unload curve has a lower magnitude of strains than the loading curve at the same applied stresses as illustrated in the fifth cycles in Fig. 3a.

The area of the load–unload curve or hysteresis shows a statistically significant increase with cycles ($p < 0.05$) up to the fourth cycle. As the maximum stress in each load/unload loop increases, the loops not only become taller (owing to the increase in stress),

Table 2
Correlation coefficients for pairs of variables examined; type-I error probabilities are indicated by boldface values, which are significant at $p < 0.01$; boldface and italicized values significant at $0.01 < p < 0.05$, and $p > 0.1$ for the remaining.

Correlation coefficients	E^{app}_{HAP}	E	V_{HAP}	V_{coll}	Apparent density	HAP intensity index	Microstructure
E^{app}_{HAP}	**1**						
E	0.10	**1**					
V_{HAP}	***0.42***	***0.83***	**1**				
V_{coll}	−0.07	***−0.83***	***−0.47***	**1**			
Apparent density	0.33 (>0.05)	***0.86***	***0.96***	***−0.48***	**1**		
HAP intensity index	***0.47***	0.03	0.11	−0.02	0.01	**1**	
Microstructure	−0.33	***−0.73***	***−0.70***	***0.74***	***−0.64***	−0.31	**1**

but also become wider. This suggests that, with increase in cycles, the degree of viscoelastic or permanent deformation in the collagen phase increases. No significant difference is observed between the hysteresis of the samples tested at RT and BT, for a given stress. The effect of temperature has been studied in creep and fracture toughness tests, where creep rates were found to increase [85] and fracture toughness was found to decrease [67] with an increase in the testing temperature. This has been suggested to occur as a result of the weakening of the bonds between the collagen molecules with increase in temperature thus weakening the material. During long-term creep tests (as compared with the present load/unload tests where the maximum stress is not maintained for long times), the viscoelastic deformation of the collagen phase takes place to a greater extent, because the durations for which the stresses are held constant are sufficient to observe such response. In those cases, the effect of temperature can be clearly distinguished [85]. However, in monotonic loading tests such as those used in the present study, each stress is held constant for ~1.5 min, during which the measurements are made at all ten locations. This duration is too short to observe any significant change in the accumulated viscoelastic strain of collagen, and thus the hysteresis effect, due to temperature.

Further, the fact that there is no statistically significant difference between the E^{app}_{HAP} values at 27 and 37 °C is not surprising. The stiffness of the composite is largely determined by the HAP phase [86,87], where even a small change in the properties (increased compliance with temperature as a result of weakening of bonds [67]) of the collagen matrix would not significantly change the load carried by the HAP. The large difference between the Young's moduli of the bulk phases of HAP (114 GPa) and collagen (1 GPa) [10,50] results in an insignificant change in the E^{app}_{HAP} values as a result of a decrease, even a large one in relative terms, in the modulus of collagen [39,45].

4.1.2. Residual strains

As shown in Fig. 3b, the residual strain magnitude in the HAP phase generally increases with the number of cycles (and the peak stress) for most of the samples tested at all the measurement locations. Initial residual strains in HAP with a similar sign and magnitude have been found in other bone samples, using X-rays [8,32,88]. These pre-strains can also improve resistance to fracture, and may develop in response to the loading history of the bone, which in turn is location dependent [88–91]. The increase in the compressive residual strain magnitude of HAP during loading/unloading also suggests accumulation of irrecoverable deformation in the collagen phase with increase in cycles. As the deformation proceeds, the collagen phase accumulates greater compressive plastic strains at zero stress, since on unloading only the elastic strains are recovered. This results in a net compressive residual plastic strain on the overall composite, which in turn subjects the embedded HAP phase to greater compressive elastic strains upon unloading to zero stress. This behavior is similar to that of a particulate-reinforced composite, where plastic deformation in the matrix results in an increase in transfer of stress to the reinforcement [92,93]. The lack of change in HAP residual strains with changing temperature may stem from the short duration for which the maximum stresses are maintained constant (and during which viscoelastic strains in the collagen phase are accumulated), preventing clear distinction between the behavior at RT and BT.

4.2. Repeatability study

4.2.1. HAP volume fraction

The apparent HAP moduli E^{app}_{HAP} do not vary significantly between the anterior and posterior quadrants, whereas the E^{app}_{HAP} values at the medial quadrant are found to be significantly greater than those at the lateral quadrants. Within the anterior region, the anterio-medial showed higher E^{app}_{HAP} values than in the anterio-lateral region. Taking into consideration the bending moments experienced in vivo by the animal, the body weight is predominantly applied to the femoral head, which is on the medial side of the femur. This produces a greater bending moment in the medial–lateral plane than the anterior–posterior plane, since that moment is resisted by the knee joint [94,95]. Thus, greater compressive strains will be produced in the medial than the lateral side of the femur, depending on the position along the femoral shaft from the femoral head. To resist the greater compressive stresses, this region will have greater HAP volume fractions, and thus lower average HAP strains (ε_{HAP}) for a given applied stress, since there are more HAP crystals to share the applied stress (σ_{app}). This in turn results in higher E^{app}_{HAP} values (given its definition as $\sigma_{app}/\varepsilon_{HAP}$) as seen here; higher HAP volume fractions also results in higher Young's modulus E values. However, the positive correlation between E^{app}_{HAP} and HAP volume fraction is much weaker (yet significant) than that between E and HAP volume fraction. This difference arises because the determination of HAP volume fractions by TGA carries uncertainties that are difficult to quantify, because the small TGA samples are cut from the larger samples after mechanical tests, from a region which corresponds only approximately to the region irradiated by the beam. Thus, the overall sample modulus E, which accounts for the average sample volume fraction, shows better correlation with the overall HAP volume fraction. The expected negative correlation between the E values and collagen volume fraction suggests that an increase in the fraction of the more compliant collagen phase (which entails a decrease in the volume fraction of the stiffer HAP phase) results in a decrease in the overall sample modulus. The poor correlation between E^{app}_{HAP} and E is also a result of the difference between the scales of measurement, averaged over a very small volume ($0.0075\ mm^3$) in the first case vs over the whole sample volume ($60\ mm^3$) in the latter case. The intrinsic variability between E^{app}_{HAP} for various locations within a single sample is at an average value of 15%. Additionally, the lack of a difference between E^{app}_{HAP} of locations measured radially, from the periosteum to the endosteum,

could be because the different samples were taken at slightly different distances from the edges of the femur thickness. This would then average out any variations that might be present.

The HAP intensity index is a measure of the fraction of all HAP crystals that contribute to the (00.2) peak diffraction intensity. This index correlates well with E^{app}_{HAP}, which takes into account only those HAP crystals along the loading direction that produce the diffracted intensity. However, the intensity index does not correlate well with the sample HAP volume fraction, because it does not contain information about those HAP crystals that are not correctly oriented for Bragg diffraction. Also, the intensity is evaluated over a volume (0.0075 mm^3) much smaller than that used for the TGA measurement (2.5 mm^3). This could increase the uncertainty in the comparison.

4.2.2. Density and microstructure

The apparent density is also found to affect the apparent moduli of the samples. The apparent density gives an indication of porosity to some extent only, since it is also affected by the HAP and collagen content in the sample. However, no direct measurement of porosity was made. The microstructure index (which takes values between zero for fully plexiform and unity for fully Haversian) is also negatively correlated with density, implying that Haversian bone is less dense than plexiform bone as consequence of the lower mineral content [96]. Both E and E^{app}_{HAP} values increase with an increase in sample apparent density and decrease with increase in sample microstructure index (or increase in the Haversian bone content in the samples). An increase in the HAP volume fraction and decrease in the collagen volume fraction results in an increase in the apparent density, as suggested by the positive correlation in Table 1, since HAP has a greater density than collagen. Thus, the increase in E^{app}_{HAP} and E is as expected.

The osteonal or Haversian type of structure has lamellae units arranged in concentric cylinders around a central Haversian canal, which is oriented along the longitudinal direction of bone, which is also the direction of loading in these experiments (within 0–10°) [38,75]. The individual lamellae in osteonal bones are arranged in a spiral fashion with respect to the Haversian canal, with the orientation of the fibrils varying from 0 to 90°, changing in a sequence of ~5–25° [38]. Plexiform structure has units of lamellae predominantly aligned along the bone longitudinal axis [97]. Thus, there are more longitudinally oriented HAP crystals within a particular sampled volume in the plexiform structure than in the Haversian structure. The presence of more longitudinally oriented HAP crystals will result in lower average strains on the HAP crystals and higher E^{app}_{HAP} values, as seen here. More longitudinally oriented HAP crystals will also result in greater stiffness in the longitudinal direction, as seen in the E values [87]. Here too, the bulk measurement (E) over a volume of 60 mm^3 exhibits a better correlation with the apparent density, which is over the same volume, than E^{app}_{HAP}, which is a local measurement over a much smaller volume of 0.0075 mm^3. However, there is a chance that the specific region which the X-ray beam samples has a significantly higher porosity in certain samples owing to the presence of a large number of void spaces, such as Haversian canals, lacunae, blood vessels and resorption spaces or lower HAP content. This would result in locally higher strains on the HAP crystals and correspondingly lower apparent moduli.

The results from this experimental study of variations in the load transfer behavior between samples taken from different locations in the same bone have shown that E^{app}_{HAP} values are well correlated with the differing HAP volume fraction and apparent density of the samples, and to some extent by the microstructure of the sample. Correlation is also found between the Young's modulus, which is a bulk measure of stiffness, and all the above factors. In general, the bulk measurements of Young's modulus, apparent density and microstructure, and the smaller-scale (over ~1.5 mm^3) measurement of HAP volume fraction were highly correlated with each other compared with the much more local measurement (over ~0.0075 mm^3) of the apparent modulus. Further studies with samples taken from locations along the whole length of the femur are of interest, as the physiological stresses (and thus presumably the structure and properties) vary according to position with respect to the femoral head and the knee joint.

5. Conclusions

This paper reports an in situ investigation of the compressive mechanical response of bovine femur, performed by nanoscale measurements of the HAP elastic strain using synchrotron XRD and macroscopic measurements of the microstructure, Young's modulus and phase volume fractions in the sample. The main results are summarized below.

1. A linear relationship between applied stress and elastic HAP strain holds up to stresses of −70 MPa, and the slope of this plot during loading—the HAP apparent modulus E^{app}_{HAP}—measures the extent of load transferred from the collagen matrix to the HAP phase.
2. Series loading/unloading cycles with increasing maximum stress from −30 to −100 MPa does not lead to a systematic change in E^{app}_{HAP} with increasing number of loading cycles, indicating that no permanent damage at the HAP–collagen interface is produced. Temperature does not affect the load partitioning behavior between the two phases: the HAP apparent modulus is not significantly different between 37 °C and 27 °C, indicating that this property is primarily determined by the HAP phase whose properties remain unaffected by this change in temperature, despite changes in the collagen matrix, which becomes more compliant owing to weakening of bonds at a higher temperature.
3. Hysteresis between the loading and unloading branches of the applied stress vs elastic strain curves develops with increasing number of load–unload cycles. A possible explanation is the sliding of collagen molecules, resulting in irreversible deformation and strain energy dissipation during the load transfer between HAP and collagen. Hysteresis is not affected by the temperature change from 27 °C to 37 °C, showing that the stress is not applied long enough to induce significant viscoelastic creep response in the collagen. The residual strains present after unloading in the HAP phase increase with increase in cycles, probably owing to the accumulation of plastic strains in the collagen matrix from loading up to high stresses of −100 MPa.
4. Variations in the load transfer behavior among samples taken from different locations within a femur cross section were observed, where the apparent HAP modulus was found to be greater at the anterio-medial end compared with the anterio-lateral end of the femur. The variations in the apparent HAP modulus and the Young's modulus are correlated with significant variations in the bone HAP volume fraction, its apparent density and its microstructure.

Acknowledgements

The authors thank Prof. L. Catherine Brinson, Dr. Alix Deymier-Black and Mr. Fang Yuan (NU) for numerous useful discussions throughout this work. Dr. Alix Deymier-Black (NU) and Dr. John Okasinski (APS) are also acknowledged for their help with the experiments at the Advanced Photon Source (APS). This research was performed at station 1-ID of XOR-APS. Use of the APS was

supported by the US Department of Energy, Office of Science, Office of Basic Energy Sciences, under Contract No. DE-AC02-06CH11357.

Appendix A. Figures with essential colour discrimination

Certain figures in this article, particularly Figs. 1–5, are difficult to interpret in black and white. The full colour images can be found in the on-line version, at http://dx.doi.org/10.1016/j.actbio.2012.03.036.

References

[1] Weiner S, Wagner HD. The material bone: structure–mechanical function relations. Annu Rev Mater Sci 1998;28:28.
[2] Posner AS. Crystal chemistry of bone mineral. Physiol Rev 1969;49:760–92.
[3] Chen P-Y, Toroian D, Price P, McKittrick J. Minerals form a continuum phase in mature cancellous bone. Calcif Tissue Int 2011;88:351–61.
[4] Gibson LJ, Ashby MF. Cellular solids—Structure and Properties. Cambridge University Press; 1997.
[5] Jaeger C, Groom NS, Bowe EA, Horner A, Davies ME, Murray RC, et al. Investigation of the nature of the protein–mineral interface in bone by solid-state NMR. Chem Mater 2005;17:3059–61.
[6] Wilson EE, Awonusi A, Morris MD, Kohn DH, Tecklenburg MMJ, Beck LW. Three structural roles for water in bone observed by solid-state NMR. Biophys J 2006;90:3722–31.
[7] Nyman JS, Roy A, Shen X, Acuna RL, Tyler JH, Wang X. The influence of water removal on the strength and toughness of cortical bone. J Biomech 2006;39:931–8.
[8] Almer JD, Stock SR. Internal strains and stresses measured in cortical bone via high-energy X-radiation. J Struct Biol 2005;152:14–27.
[9] Rho J-Y, Spearing LK, Zioupos P. Mechanical properties and hierarchical structure of bone. Med Eng Phys 1998;20:92–102.
[10] Jager I, Fratzl P. Mineralized collagen fibirils: a mechanical model with a staggered arrangement of mineral particles. Biophys J 2000;79:1737–46.
[11] Ji B, Gao H. Elastic properties of nanocomposite structure of bone. Compos Sci Technol 2006;66:1212–8.
[12] Yuan F, Almer J, Dunand DC, Brinson LC. A new model to simulate the elastic properties of mineralized collagen fibril. Biomech Model Mechanobiol 2011;10:147–60.
[13] Hoo RP, Fratzl P, Daniels JE, Dunlop JWC, Honkimäki V, Hoffman M. Cooperation of length scales and orientations in the deformation of bovine bone. Acta Biomater 2011;7:2943–51.
[14] Novitskaya E, Chen P-Y, Lee S, Castro-Ceseña A, Hirata G, Lubarda VA, et al. Anisotropy in the compressive mechanical properties of bovine cortical bone and the mineral and protein constituents. Acta Biomater 2011;7:3170–7.
[15] Fritsch A, Hellmich C. "Universal" microstructural patterns in cortical and trabecular, extracellular and extravascular bone materials: micromechanics-based prediction of anisotropic elasticity. J Theor Biol 2007;244:597–620.
[16] Barak MM, Currey JD, Weiner S, Shahar R. Are tensile and compressive Young's moduli of compact bone different? J Mech Behav Biomed Mater 2009;2:51–60.
[17] Kulin RM, Jiang F, Vecchio KS. Effect of age and loading rate on equine cortical bone failure. J Mech Behav Biomed Mater 2011;4:57–75.
[18] Carter DR, Hayes WC. The compressive behavior of bone as a two-phase porous structure. J Bone Joint Surg 1977;59:954–62.
[19] Nyman JS, Leng H, Dong XN, Wang X. Differences in the mechanical behavior of cortical bone between compression and tension when subjected to progressive loading. J Mech Behav Biomed Mater 2009;2:613–9.
[20] Novitskaya E, Chen P-Y, Lee S, Castro-Ceseña A, Hirata G, Lubarda VA, et al. Anisotropy in the compressive mechanical properties of bovine cortical bone and the mineral and protein constituents. Acta Biomater 2011;7:3170–7.
[21] Haeffner DR, Almer JD, Lienert U. The use of high energy X-rays from the advanced photon source to study stresses in materials. Mater Sci Eng A 2005;399:120–7.
[22] Young ML, Almer JD, Daymond MR, Haeffner DR, Dunand DC. Load partitioning between ferrite and cementite during elasto-plastic deformation of an ultrahigh-carbon steel. Acta Mater 2007;55:1999–2011.
[23] Young ML, DeFouw J, Almer JD, Dunand DC. Load partitioning during compressive loading of a Mg/MgB2 composite. Acta Mater 2007;55:3467–78.
[24] Kerr M, Daymond MR, Holt RA, Almer JD. Strain evolution of zirconium hydride embedded in a zircaloy-2 matrix. J Nucl Mater 2008;380:70–5.
[25] Gupta HS, Messmer P, Roschger P, Bernstorff S, Klaushofer K, Fratzl P. Synchrotron diffraction study of deformation mechanisms in mineralized tendon. Phys Rev Lett 2004;93:158101-1–4.
[26] Puxkandl R, Zizak I, Paris O, Keckes J, Tesch W, Bernstorff S, et al. Viscoelastic properties of collagen: synchrotron radiation investigations and structural model. Philos Trans R Soc Lond B 2002;357:191–7.
[27] Folkhard W, Mosler E, Geercken W, Knorzer E, Nemetschek-Gansler H, Nemetschek T, et al. Quantitative analysis of the molecular sliding mechanism in native tendon collagen- time-resolved dynamic studies using synchrotron radiation. Int J Biol Macromol 1987;9:169–75.
[28] Mosler E, Folkhard W, Knorzer E, Nemetschek-Gansler H, Nemetschek T, Koch MHJ. Stress-induced molecular rearrangement in tendon collagen. J Mol Biol 1985;182:589–96.
[29] Sasaki N, Shukunami N, Matsushima N, Izumi Y. Time-resolved X-ray diffraction from tendon collagen during creep using synhcrotron radiation. J Biomech 1998;32:285–92.
[30] Fratzl P, Misof K, Zizak I, Rapp G, Amenitsch H, Bernstorff S. Fibrillar structure and mechanical properties of collagen. J Struct Biol 1997;122:119–22.
[31] Misof K, Rapp G, Fratzl P. A new molecular model for collagen elasticity based on synchrotron X-ray scattering evidence. Biophys J 1997;72:1376–81.
[32] Almer JD, Stock SR. Micromechanical responses of mineral and collagen phases in bone. J Struct Biol 2007;157:365–70.
[33] Stock SR, Carlo FD, Almer JD. High energy X-ray scattering tomography applied to bone. J Struct Biol 2008;161:144–50.
[34] Akhtar R, Daymond MR, Almer JD, Mummery PM. Elastic strains in antler trabecular bone determined by synchrotron X-ray diffraction. Acta Biomater 2008;4:1677–87.
[35] Gupta HS, Wagermaier W, Zickler GA, Aroush DR-B, Funari SS, Roschger P, et al. Nanoscale deformation mechanisms in bone. Nano Lett 2005;5:2108–11.
[36] Gupta HS, Seto J, Wagermaier W, Zaslansky P, Boesecke P, Fratzl P. Cooperative deformation of mineral and collagen in bone at the nanoscale. PNAS 2006;103:17741–6.
[37] Gupta HS, Wagermaier W, Zickler A, Hartmann J, Funari SS, Roschger P, et al. Fibrillar level fracture in bone beyond the yield point. Int J Fract 2006;139:425–36.
[38] Wagermaier W, Gupta HS, Gourrier A, Burghammer M, Roschger P, Fratzl P. Spiral twisting of fiber orientation inside bone lamellae. Biointer Phases 2006;1:1–5.
[39] Singhal A, Deymier-Black A, Almer JD, Dunand DC. Effect of high-energy X-ray doses on bone elastic properties and residual strains. J Mech Behav Biomed Mater 2011;4:1774–86.
[40] Deymier-Black AC, Yuan F, Singhal A, Almer JD, Brinson LC, Dunand DC. Evolution of load transfer between hydroxyapatite and collagen during creep deformation of bone. Acta Biomater 2011;8:253–61.
[41] Krauss S, Fratzl P, Seto J, Currey JD, Estevez JA, Funari SS, et al. Inhomogeneous fibril stretching in antler starts after macroscopic yielding: indication for a nanoscale toughening mechanism. Bone 2009;44:1105–10.
[42] Neil Dong X, Almer JD, Wang X. Post-yield nanomechanics of human cortical bone in compression using synchrotron X-ray scattering techniques. J Biomech 2011;44:676–82.
[43] Barth HD, Zimmermann EA, Schaible E, Tang SY, Alliston T, Ritchie RO. Characterization of the effects of X-ray irradiation on the hierarchical structure and mechanical properties of human cortical bone. Biomaterials 2011;32:8892–904.
[44] Deymier-Black AC, Almer JD, Haeffner DR, Dunand DC. Effect of freeze–thaw cycles on load transfer between the biomineral and collagen phases in bovine dentin. Mater Sci Eng C 2011;31:1423–8.
[45] Deymier-Black AC, Almer JD, Stock SR, Haeffner DR, Dunand DC. Synchrotron X-ray diffraction study of load partitioning during elastic deformation of bovine dentin. Acta Biomater 2010;6:2172–80.
[46] Almer JD, Stock SR. High energy X-ray scattering quantification of in situ-loading-related strain gradients spanning the dentinoenamel junction (DEJ) in bovine tooth specimens. J Biomech 2010;43:2294–300.
[47] Deymier-Black AC, Stock SR, Almer JD, Dunand DC. Variability in the elastic properties of bovine dentin at multiple length scales. J Mech Behav Biomed Mater 2012;5:71–81.
[48] Akhtar R, Daymond MR, Almer JD, Mummery PM. Load transfer in bovine plexiform bone determined by synchrotron X-ray diffraction. J Mater Res 2007;23:543–50.
[49] Gilmore RS, Katz JL. Elastic properties of apatites. J Mater Sci 1982; 17:1131–41.
[50] Grenoble DE, Katz JL, Dunn KL, Gilmore RS, Murty KL. Elastic properties of hard tissues and apatites. J Biomed Mater Res 1972;6:221–33.
[51] Sasaki N, Odajima S. Stress–strain curve and Young's modulus of a collagen molecule as determined by the X-ray diffraction technique. J Biomech 1996;29:655–8.
[52] Almer JD, Stock SR. Micromechanical responses of mineral and collagen phases in bone. J Struct Biol 2007;157:365–70.
[53] Weiss S, Zimmerman MC, Harten RD, Alberta FG, Meunier A. The acoustic and structural properties of human femur. J Biomech Eng 1998;120:71–6.
[54] Rho JY, Zioupos P, Currey JD, Pharr GM. Variations in the individual thick lamellar properties within osteons by nanoindentation. Bone 1999;25:295–300.
[55] Smith JW, Walmsley R. Factors affecting the elasticity of bone. J Anat 1959;93:503–23.
[56] Currey JD. Effects of differences in mineralization on the mechanical properties of bone. Philos Trans R Soc Lond B: Biol Sci 1984;304:509–18.
[57] Peterlik H, Roschger P, Klaushofer K, Fratzl P. From brittle to ductile fracture of bone. Nat Mater 2006;5:52–5.
[58] Yamato Y, Kataoka H, Matsukawa M, Yamazaki K, Otani T, Nagano A. Distribution of longitudinal wave velocities in bovine cortical bone in vitro. Jpn J Appl Phys Part 1—Regul Pap Brief Commun Rev Pap 2005;44: 4622–4.
[59] Espinoza Orías AA, Deuerling JM, Landrigan MD, Renaud JE, Roeder RK. Anatomic variation in the elastic anisotropy of cortical bone tissue in the human femur. J Mech Behav Biomed Mater 2009;2:255–63.

[60] Sansalone V, Naili S, Bousson V, Bergot C, Peyrin F, Zarka J, et al. Determination of the heterogeneous anisotropic elastic properties of human femoral bone: from nanoscopic to organ scale. J Biomech 2010;43:1857–63.
[61] Bensamoun S, Tho M-CHB, Luu S, Gherbezza J-M, de Belleval J-F. Spatial distribution of acoustic and elastic properties of human femoral cortical bone. J Biomech 2004;37:503–10.
[62] Sasso M, Haïat G, Yamato Y, Naili S, Matsukawa M. Frequency dependence of ultrasonic attenuation in bovine cortical bone: an in vitro study. Ultrasound Med Biol 2007;33:1933–42.
[63] Yamato Y, Matsukawa M, Otani T, Yamazaki K, Nagano A. Distribution of longitudinal wave properties in bovine cortical bone in vitro. Ultrasonics 2006;44:e233–7.
[64] Thomas CDL, Feik SA, Clement JG. Regional variation of intracortical porosity in the midshaft of the human femur: age and sex differences. J Anat 2005;206:115–25.
[65] Ramasamy JG, Akkus O. Local variations in the micromechanical properties of mouse femur: the involvement of collagen fiber orientation and mineralization. J Biomech 2007;40:910–8.
[66] Meunier A, Katz JL, Christel P, Sedel L. A reflection scanning acoustic microscope for bone and bone–biomaterials interface studies. J Orthop Res 1998;6:770–5.
[67] Yan J, Clifton Jr KB, Mecholsky JJ, Gower LA. Effect of temperature on the fracture toughness of compact bone. J Biomech 2007;40:1641–5.
[68] Leng H, Dong XN, Wang X. Progressive post-yield behavior of human cortical bone in compression for middle-aged and elderly groups. J Biomech 2009;42:491–7.
[69] He BB, Smith KL. Fundamental equation of strain and stress measurement using 2D detectors. In: Society of experimental mechanics' spring conference, Houston; 1998. p. 217–20.
[70] Warren BE. X-ray diffraction. Reading, MA: Addison-Wesley; 1969.
[71] Lee SC, Coan BS, Bouxsein ML. Tibial ultrasound velocity measured in situ predicts the material properties of tibial cortical bone. Bone 1997;21:119–25.
[72] Lees S, Heeley JD, Cleary PF. A study of some properties of a sample of bovine cortical bone using ultrasound. Calcif Tissue Int 1979;29:107–17.
[73] Buskirk WCV, Cowin SC, Ward RN. Ultrasonic measurement of orthotropic elastic constants of bovine femoral bone. J Biomech Eng 1981;103:67–72.
[74] Lozano LF, Pena-Rico MA, Heredia A, Octolan-Flores J, Gomez-Cortes A, Velazquez R, et al. Thermal analysis study of human bone. J Mater Sci 2003;38:4777–82.
[75] Martin RB, Burr DB, Sharkey NA. Skeletal tissue mechanics. Springer Verlag; 1998.
[76] Mano JF. Viscoelastic properties of bone: mechanical spectroscopy studies done on a chicken model. Mater Sci Eng 2005;C 25:145–52.
[77] Yamashita J, Li X, Furman BR, Rawls HR, Wang X, Agrawal CM. Collagen and bone viscoelasticity: a dynamic mechaznical analysis. J Biomed Mater Res 2002;63:31–6.
[78] Winwood K, Zioupos P, Currey JD, Cotton JR, Taylor M. Strain patterns during tensile, compressive, and shear fatigue of human cortical bone and implications for bone biomechanics. J Biomed Mater Res A 2006;79:289–97.
[79] Gupta HS, Fratzl P, Kerschnitzki M, Benecke G, Wagermaier W, Kirchner HOK. Evidence for an elementary process in bone plasticity with an activation enthalpy of 1 eV. JR Soc Interf 2007;4:277–82.
[80] Fantner GE, Hassenkam T, Kindt JH, Weaver JC, Birkedal H, Pechenik L, et al. Sacrificial bonds and hidden length dissipate energy as mineralized fibrils separate during bone fracture. Nat Mater 2005;4:612–6.
[81] Thompson JB, Kindt JH, Drake B, Hansma HG, Morse DE, Hansma PK. Bone indentation recovery time correlates with bond reforming time. Nat Mater 2001;414:773–6.
[82] Walsh WR, Guzelsu N. Compressive properties of cortical bone: mineral–organic interfacial bonding. Biomaterials 1994;15:137–45.
[83] Hubner W, Blume A, Pushnjakova R, Dekhtyar Y, Hein H-J. The influence of X-ray radiation on the mineral/organic matrix interaction of bone tissue: an FT-IR microscopic investigation. Int J Artif Organs 2005;28:66–73.
[84] Sasaki N, Odajima S. Elongation mechanism of collagen fibrils and force–strain relations of tendon at each level of structural hierarchy. J Biomech 1996;29:1131–6.
[85] Rimnac CM, Petko AA, Santner TJ, Wright TW. The effect of temperature, stress and microstructure on the creep of compact bovine bone. J Biomech 1993;26:219–21.
[86] Burstein AH, Zika JM, Heiple KG, Klein L. Contribution of collagen and mineral to the elastic–plastic properties of bone. J Bone Joint Surg 1975;57:956–61.
[87] Hasegawa K, Turner CH, Burr DB. Contribution of collagen and mineral to the elastic-anisotropy of bone. Calcif Tissue Int 1994;55:381–6.
[88] Giri B, Tadano S, Fujisaki K, Todoh M. Understanding site-specific residual strain and architecture in bovine cortical bone. J Biomech 2008;41:3107–15.
[89] Goodyear SR, Gibson IR, Skakle JMS, Wells RPK, Aspden RM. A comparison of cortical and trabecular bone from C57 black 6 mice using Raman spectroscopy. Bone 2009;44:899–907.
[90] Ascenzi A, Benvenuti A. Evidence of a state of initial stress in osteonic lamellae. J Biomech 1977;10:447–53.
[91] Ascenzi M-G. A first estimation of prestress in so-called circularly fibered osteonic lamellae. J Biomech 1999;32:935–42.
[92] Allen AJ, Bourke MAM, Dawes S, Hutchings MT, Withers PJ. The analysis of internal strains measured by neutron diffraction in Al/SiC metal matrix composites. Acta Metall Mater 1992;40:2361–73.
[93] Withers PJ, Stobbs WM, Pedersen OB. The application of the eshelby method of internal stress determination to short fibre metal matrix composites. Acta Metall 1989;37:3061–84.
[94] Taylor ME, Tanner KE, Freeman MAR, Yettram AL. Stress and strain distribution within the intact femur: compression or bending? Med Eng Phys 1996;18:122–31.
[95] Rudman KE, Aspden RM, Meakin JR. Compression or tension? The stress distribution in the proximal femur. Biomed Eng Online 2006;5:7.
[96] Carter DR, Hayes WC, Schurman DJ. Fatigue life of compact bone—II. Effects of microstructure and density. J Biomech 1976;9:211–8.
[97] Katz JL, Yoon HS. The structure and anisotropic mechanical properties of bone. IEEE Trans biomed eng 1984;BME-31:878–84.